Pressure-driven tunable properties of the small-gap chalcopyrite topological quantum material ZnGeSb$_2$: A first-principles study

Surasree Sadhukhan,[1,*] Banasree Sadhukhan [2,3,*,†] and Sudipta Kanungo [1,‡]

[1]*School of Physical Sciences, Indian Institute of Technology Goa, 403401 Ponda, India*
[2]*KTH Royal Institute of Technology, AlbaNova University Center, SE-10691 Stockholm, Sweden*
[3]*Institute for Theoretical Solid State Physics, IFW Dresden, Helmholtzstrasse 20, 01069 Dresden, Germany*

Search for new topological quantum materials is the demand of time and the theoretical prediction plays a crucial role besides the obvious experimental verification. Divination of topological properties in already well-known narrow gap semiconductors is a flourishing area in quantum material. In this view we revisited the semiconductor compound in the chalcopyrite series, with a very small gap near the Fermi energy. Using the density functional theory-based first-principles calculations, we report a strong topologically nontrivial phase in chalcopyrite ZnGeSb$_2$, which can act as a model system of strained HgTe. The calculations reveal the nonzero topological invariant (Z_2), the presence of Dirac cone crossing in the surface spectral functions with spin-momentum locked spin texture. We also study the interplay between the structural parameters and electronic properties, and report the tunable topological properties due to a very small band gap, from nontrivial to trivial phase under the application of moderate hydrostatic pressure within ≈ 7 GPa. A small modification of a lattice parameter is enough to achieve this topological phase transition which is easily accomplished in an experimental laboratory. The calculations show that a discontinuity in the tetragonal distortion of noncentrosymmetric ZnGeSb$_2$ plays a crucial role in driving this topological phase transition. Our results are further collaborated with a low energy $\mathbf{k} \cdot \mathbf{p}$ model Hamiltonian to validate our *abinitio* findings. We showed that the evaluation of the model band energy dispersion under the hydrostatic pressure is consistent with the obtained results.

I. INTRODUCTION

The topological phase of matter is a novel quantum phase apart from the conventional metal or ordinary insulator, where the quantum degrees of freedom play a tremendous role. Intense research efforts have been invested in understanding, manipulating, and predicting the new topological quantum materials from fundamental scientific interests and technological aspects. In this search process, various kinds of systems have been explored starting from the magnetic systems, semiconductors, semimetals, cold atoms, nanomaterials, as well as the photonic crystals in the last decade for the search of novel exotic topological phenomena [1–11]. In this current scenario, designing and tuning any type of topological features employing topological phase transition by experimentally achievable external perturbation is indispensable for the growth of this field. For such progress, the theoretical studies played a significant role in the last few years due to the advancement of the computational methodology [12–15].

Topological insulators (TIs) are the three-dimensional counterparts of two-dimensional quantum spin Hall insulators [16–19] that are characterized by a nontrivial topological Z_2 invariant associated with the gapped bulk electronic structure [20–25] and spin-momentum locked gapless surface or edge states with an odd (even) number of massless Dirac cones which leads to strong (weak) TIs classification. They have inverted band ordering due to the switching of bands with opposite parity at high symmetry momenta of the Brillouin zone (BZ) around the Fermi level compared to their topological trivial phase.

It is of particular interest to identify materials for which the band contribution from opposite parity orbitals can be tuned, and topological properties can be switched via topological phase transitions. In principle, the phase transitions between topological trivial and nontrivial states can be achieved by the external perturbations such as tuning the electronegativity or tuning the strength of spin-orbit coupling (SOC) via substituting proper elements [19,24,26], by alloying composition or chemical doping [27–29], or by uniform hydrostatic pressure and strain. Pressure-induced topological phase transition have been identified in layered materials [30,31], BiTeI [32,33], Pb$_{1-x}$Sn$_x$ [34], polar semiconductors BiTeBr [35], topological crystalline insulators [36], vdW materials MoTe$_2$ [37], elemental Te [38], chalcogenides [39], and chalcopyrite compounds like CdGeSb$_2$ and CdSnSb$_2$ [40].

In recent advancement of composite quantum compounds [41], where multiple quantum phenomena occurs simultaneously, the ternary chalcopyrites of composition I-III-VI$_2$ and II-IV-V$_2$ become very much relevant as it provides a unique platform to host multiple topologically exotic phases [42] along with the thermoelectricity [43,44], superconductivity [45], topological shift current [51], spin

---
[*]These authors contributed equally to this work.
[†]b.sadhukhan@ifw-dresden.de
[‡]sudipta@iitgoa.ac.in

crossover phenomena [46], antiferromagnetism, and many more. Few of them can be realized as the topological insulator or Weyl semimetals in their native states [42,47]. Room temperature ferromagnetism can also be found in chalcopyrites by magnetic doping in addition to the topological nontrivial phases [48–50]. Very recently, photovoltaic phenomena related to the Berry phase of the constituting electronic bands were established in chalcopyrite compound $ZnSnP_2$ [51]. Not only in the field of condensed matter physics, but small-gap chalcopyrites have also been investigated in detail in the context of detection of the dark matter of the universe [52]. The wide availability of chalcopyrite semiconductors and the control of topological order via tuning lattice parameters, hydrostatic pressure, and chemical doping opens new possibilities for this family's ideal platform to further investigate the novel topological quantum phenomena.

Motivated by the above issues, we focused here on a chalcopyrite compound $ZnGeSb_2$ which has a very small positive ($E_{\Gamma_6} - E_{\Gamma_8}$) band gap. From the literature it is known that the $ZnGeSb_2$ has been investigated in the context of the thermoelectricity [43,44], photovoltaic effect [51], anion heterojunction [53], and topological phases [42]. However, the study on the topological properties of $ZnGeSb_2$ is minimal and not conclusive. One of the reports [42] show it as a trivial semiconductor but far from indenting topological signatures. Another piece of literature says it has a massive Dirac state [43]. From the perspective of the composite quantum materials, it will be very interesting if one can find conclusive evidence of the topological phases in this material, which will open up a distinctive playground to understand the interplay of the thermoelectric properties and the topological properties of the bands. Very recently efforts have been invested in this direction to understand this interplay in the different classes of materials [54–59], however, they are very limited and plenty of scopes are there.

Structurally these chalcopyrites can be viewed as strained HgTe, which crystallizes in the zinc-blende lattice structure. The atomic positions (Wyckoff positions) in a material depend on the symmetry of the systems followed by the space group of the materials family. Chalcopyrite series compounds are such materials where the Wyckoff positions depend on the constituent atom in that material. In this series of materials, each anion has two different cations as nearest neighbors. This leads to the structural distortion compared to the ideal HgTe structure, which is determined by both the lattice parameter's ratio and the internal displacement of the anions (anion shift) towards one of the cations as compared to the ideal zinc-blende sites. So both the lattice parameters and atomic positions are important parameters to determine its ground state structure and, consequently, the properties whether it is in a topological nontrivial or trivial state.

In the present study we have investigated the topological signatures of $ZnGeSb_2$ in great detail for the ambient phase and the high-pressure phase. After the identification of the pressure-driven novel superconducting phase in the chalcopyrite material $ZnSiP_2$ [45], it would be worth it to do a pressure-driven investigation of the topological phases for the chalcopyrite family, specifically for $ZnGeSb_2$, where the electronic band gap is very small and susceptible under pressure. Our calculated results show that the parent ambient phase of $ZnGeSb_2$ is a strong topological insulator with a negative band gap, nonzero topological index (Z_2 number), odd numbers of Dirac crossing in the surface function, and spin-momentum locking with 2π Berry phase. By the application of the uniform moderate hydrostatic pressure (≈ 7 GPa), the band gap between Γ_6 and Γ_8 gets flipped compared to the ambient pressure phase and undergoes a topological phase transition from the topological insulating phase to the trivial band semiconductor. We also correlate the topological phase transition with the structural modification in terms of the delicate balance in the lattice parameters and the anion position displacements, which translates into the variation of the tetragonal distortion of the crystal. We found that although there is no structural phase transition, the discontinuous jump of the tetragonal distortion (δu) and the anion displacement (x) happens exactly at the phase transition pressure. We also analyzed our results in terms of the low energy $\mathbf{k} \cdot \mathbf{p}$ model Hamiltonian approach considering the symmetry of the systems. We found that one can understand the topological phase transition under pressure associated with the change in the sign of the mass terms in the Hamiltonian, which is consistent the $ab-initio$ band inversion results. Since this material is not yet synthesized experimentally, it is worth doing a detailed theoretical investigation to understand the physical properties, which will act as a guiding factor for the experimentalist and, as per the best of our knowledge, the detailed microscopic understanding of the possible signatures of the topological phases of $ZnGeSb_2$ are still lacking in the literature.

II. CALCULATIONS METHODOLOGY

Density functional theory (DFT) based electronic structure calculations were performed using the local orbital basis set in the full potential framework as implemented in the FPLO code [67,68] as well as for structural aspects through the plane-wave basis set based on a pseudopotential framework as incorporated in the Vienna *abinitio* simulation package (VASP) [61,62]. The generalized gradient exchange-correlation approximated (GGA) functional was employed following the Perdew-Burke-Ernzerhof (PBE) prescription [60]. We also crosschecked our calculation using a different exchange correlation functional, such as local density approximation (LDA), and found that, though the optimized lattice parameters are different than the PBE calculations, however, the results regarding the topological features of the band structure remains unaffected. For the plane-wave basis, a 600 eV cutoff was applied. Since the experimental crystal structure is not available for this material, the structural optimization was performed by relaxing both a and c lattice parameters and the internal atomic positions (Wyckoff positions) of all the atoms toward the equilibrium until the Hellmann-Feynman force becomes less than 0.001 eV/Å. We also crosschecked the obtained optimized lattice parameters (a and c) and the Wyckoff positions through the energy minimization method as shown in Fig. 4. A k-point mesh of $6 \times 6 \times 4$ in the Brillouin zone was used for the calculations. All the structures were optimized and the self-consistent calculations were converged with a tight convergence threshold for the energy (10^{-7} eV).
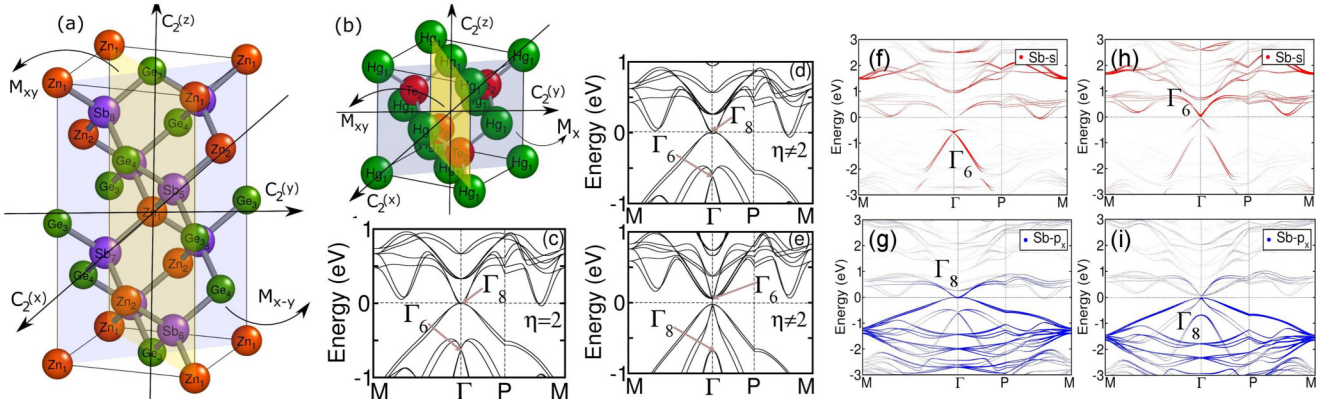
FIG. 1. Unit cell of the (a) body-centered tetragonal ZnGeSb$_2$ and (b) HgTe. The associated symmetry axes and planes are also shown by line and shade, respectively. Calculated GGA+SOC band structures along the high symmetry line in the BZ with (c) artificial structure of ZnGeSb$_2$, where $\eta = 2$, with $\delta u = 0$, and (d) and (e) with real distorted tetragonal crystal of ZnGeSb$_2$ for ambient structure and high-pressure structure, respectively. (f)–(i) The calculated GGA+SOC orbital projected band structure of Sb atoms. (f) and (g) Parent phase (topological nontrivial), (h) and (i) High-pressure (topological trivial) phases of ZnGeSb$_2$, respectively, for the the projected bands of Sb-$5s$ and Sb-$5p_x$. The bands for the Sb-$5p_y$ and Sb-$5p_z$ orbitals are similar to Sb-$5p_x$ for both phases, shown in Fig. 6. Γ_6 and Γ_8 band characters are marked in the figure and the band inversion in topological phase happens between $5s$ (Γ_6) and $5p$ (Γ_8) orbitals at the Γ point in the BZ. Fermi energy set at zero on the energy axis.

The tight-binding model is constructed with the Wannier function basis set to investigate its topological properties. Wannierization is an energy selective method that produces the low energy, few orbital Hamiltonian defined in the effective Wannier function basis by integrating out the degrees of freedom that are not of interest through the renormalization method. For our downfolding calculations, therefore, we have kept only Sb s and p orbitals as active degrees of freedom in the projection and downfolded all the other degrees of freedom. The Wannier interpolated bands, Z_2 invariant, Wannier charge centers (WCCs), surface states, and the spin textures were calculated using Wannier90 [63–65] and WannierTool [66] starting from full DFT calculations. The reliability of the calculations and the results has been crosschecked in the other basis set using the full potential method as implemented in FPLO [67,68]. We also calculate the Z_2 invariant using the Wannier-center algorithm within FPLO (full-potential local-orbital minimum basis) [67,68]. The obtained electronic structure resulting from two different basis sets are consistent with each other, confirming the robustness of our analysis. We analyzed our results through the model Hamiltonian approach based on the the the the $\mathbf{k} \cdot \mathbf{p}$ methodology [69–72] using the symmetries of the system. This 4×4 model Hamiltonian provides an accurate description of the valence and the conduction band near the Fermi energy in the high symmetry k points of the BZ.

III. CRYSTAL STRUCTURE AND SYMMETRY

ZnGeSb$_2$ crystallize in the body-centered tetragonal structure, which in the chalcopyrite phase has a space group $I\bar{4}2d$ (No. 122). Structurally it is a superlattice of a zinc-blende structure, like ideal HgTe, doubling the unit cell along the crystallographic z direction. In the ZnGeSb$_2$, each anion Sb has two Zn and two Ge cations as nearest neighbors as shown in Fig. 1(a). Due to dissimilar atoms as neighbors, the anion acquires an equilibrium position closer to one pair of cations

than to the other. The Wyckoff positions of the different atoms in the tetragonal unit cell are: Zn atom at (0, 0, 0); Ge atom at (0, 0, 0.5), and Sb atom at (x, 0.25, 0.125), where x is the anion displacement parameter. The full structural optimization calculations and the energy minimization of the structural parameters (shown in Fig. 4) gives us the lattice parameters $a = 6.20$ Å, $c = 12.33$ Å, and the anion displacement parameter turns out to be $x = 0.2454$. Since this compound is not synthesized experimentally yet, it is very important to examine the thermodynamic and dynamical stability of the optimized structure. To the best of our knowledge, none of the previous calculations of the materials analyzed this stability factor through the phonon modes. The calculated phonon density of states with an absence of any imaginary frequency phonon mode and the Helmholtz free energy, as shown in the Fig. 5, confirm the stability of the structures both dynamically and thermodynamically. The internal displacement of the anion in chalcopyrite compounds of general form ABC$_2$ is defined as $\delta u = (R_{AC}^2 - R_{BC}^2)/a^2$ where R_{AC} and R_{BC} are the bond lengths between the anion C and its two nearest A and B cations [47], respectively. In the most general case of chalcopyrite, $x \neq 0.25$ and $\eta \neq 2$, where $\eta = c/a$, a and c are the lattice parameters. and δu measures the tetragonal distortion and is responsible for the breaking of the inversion symmetry in ZnGeSb$_2$. The noncentrosymmetric ZnGeSb$_2$ crystal has two twofold screw rotation symmetries along $C_2(x)$ and $C_2(y)$, respectively, and two glide mirror symmetries M_{xy} and M_{x-y}, in addition to that of the pure twofold rotational symmetry along $C_2(z)$.

In the case of the binary compound with zinc-blende structure (i.e., the cubic symmetry), the x is 0.25 and $\eta = c/a = 1$. The zinc-blende HgTe superlattice can be regarded as a model chalcopyrite like ABC$_2$ with A = B = Hg, C = Te, $\eta = 2$, and $\delta u = 0$. Interestingly, in the chalcopyrite, the cubic symmetry is broken due to the tetragonal distortion ($\eta \neq 1$) and the internal displacement ($\delta u \neq 0$). Therefore, ZnGeSb$_2$ can be thought of as the strained HgTe [see Fig. 1(b)].

IV. ELECTRONIC BAND STRUCTURE

The calculated electronic SOC band structures are shown in Figs. 1(c)–1(e) along the high symmetry lines in the BZ with Γ point which is the point of interest to study the topological features in our case. In an ideal zinc-blende structure with cubic symmetry as found in HgTe ($\delta u = 0$, $x = 0.25$, $\eta = 1$), the p orbital symmetric fourfold degenerate Γ_8 states of total angular momentum $J = \frac{3}{2}$ lies above the s orbital symmetric twofold degenerate Γ_6 and Γ_7 states of total angular momentum of $J = \frac{1}{2}$.

To understand the band topology relating to the breaking of symmetry and tetragonal distortion, we did a model calculation by considering a hypothetical structure, where anion (Sb) Wyckoff position $x = 0.25$ and setting $\eta = 2$ ($\eta = c/a$, where a and c are the exact lattice parameters of ZnGeSb$_2$ obtained through the structural optimization in the ambient structure) as shown in Fig. 1(c). In this hypothetical structure, $\delta u = 0$, i.e., without tetragonal distortion and the same space group, keeps the constant point group symmetry of the structure. The fourfold degeneracy of Γ_8 is protected when $\eta = 2$. The Dirac cone type feature at Γ point at the Fermi energy, is similar to that of the case of HgTe with $\eta = 2$. However, the ZnGeSb$_2$ formed in a chalcopyrite structure of tetragonal unit cell where $\eta \neq 2$ and $x \neq 0.25$, the fourfold degenerate light-hole and heavy-hole subbands of Γ_8 states were lifted and typically formed the top set of the valence bands and the bottom set of the conduction bands at Γ point above Fermi energy as shown in Fig. 1(d). In ZnGeSb$_2$, $E_{\Gamma_6} - E_{\Gamma_8}$ (≈ -0.6 eV) is less than zero, which indicates its topological nontrivial nature in the native ambient structure phase. Since the local gap at Γ point between Γ_6 and Γ_8 bands is very tiny, any moderate level of external perturbation may flip the band ordering at the Γ point in the BZ. With this motivation, we applied uniform hydrostatic pressure to the parent structure of ZnGeSb$_2$ keeping the space group symmetry ($I\bar{4}2d$) unaltered.

The calculated band structure with SOC in the high-pressure case is shown in Fig. 1(e). We found that at about moderate uniform hydrostatic pressure (≈ 7 GPa), the topological band ordering at Γ point in the BZ gets flipped, i.e., after applying pressure, Γ_6 and Γ_8 form the bottom of the conduction band and the top of the valence band, respectively, making the $E_{\Gamma_6} - E_{\Gamma_8} > 0$ with band gap nearly $+0.2$ eV as shown in Fig. 2(c). Therefore, ZnGeSb$_2$ undergoes topological phase transition from topological nontrivial to trivial topological phase by the flipping of Γ_6 and Γ_8 bands ordering as a function of applied external uniform hydrostatic pressure like perturbation. To understand the evolution of band structure across the topological phase transition mediated through hydrostatic pressure, we compared the orbital projected band structures for the parent (topologically nontrivial) and high-pressure (topologically trivial) phase of ZnGeSb$_2$ in Figs. 1(f)–1(i). The calculations show that the Sb atom's contribution dominates near the Fermi energy, with the small contribution of Ge atoms. We have shown the orbital contribution of Sb atoms of ZnGeSb$_2$ for both parent and high-pressure phases for the sake of clarity to identify the band inversion. In the parent structure phase, at the Γ point of the BZ, the valence band maximum (VBM) has the major contribution from the Sb-$5s$ orbital, forming the Γ_6 bands, whereas the conduction band
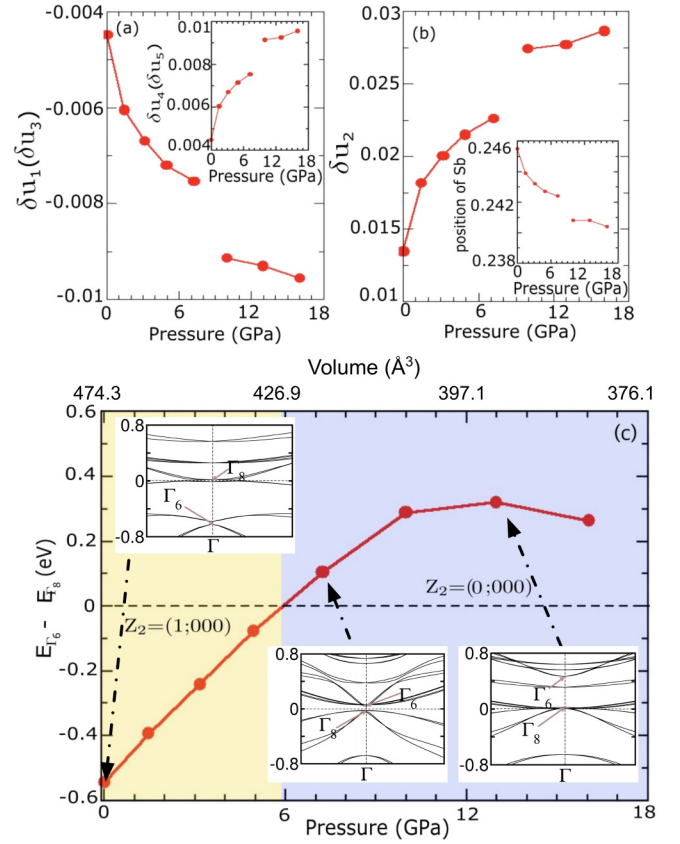

FIG. 2. (a) and (b) The variation of the tetragonal distortions δu as a function of applied external hydrostatic pressure. The inset in (b) represents the deviation of Sb atomic position from ideal $x = 0.25$ as a function of external pressure. Structural data are calculated via structural optimization at the DFT level. $\delta u_1 = \frac{(Zn_1 - Sb_5)^2 - (Ge_3 - Sb_5)^2}{a^2}$, $\delta u_2 = \frac{(Zn_2 - Sb_5)^2 - (Ge_4 - Sb_6)^2}{a^2}$, and $\delta u_3 = \frac{(Zn_2 - Sb_8)^2 - (Ge_4 - Sb_7)^2}{a^2}$. $\delta u_4 = \frac{(Zn_2 - Sb_5)^2 - (Ge_4 - Sb_7)^2}{a^2}$ and $\delta u_5 = \frac{(Zn_2 - Sb_8)^2 - (Ge_4 - Sb_6)^2}{a^2}$. (c) The calculated $E_{\Gamma_6} - E_{\Gamma_8}$ and Z_2 invariant quantities ($\gamma; \gamma_1 \gamma_2 \gamma_3$) of ZnGeSb$_2$ as a function of applied hydrostatic pressure (and corresponding volume of the unit cell) show the topological phase transition at ≈ 6–7 GPa. It is in topological nontrivial phase for $E_{\Gamma_6} - E_{\Gamma_8} < 0$ and topological trivial phase for $E_{\Gamma_6} - E_{\Gamma_8} > 0$. Insets show the Γ_6 and Γ_8 bands positioning before and after phase transition.

minimum (CBM) has the major contribution from Sb-$5p_x$ and Sb-$5p_y$ and a minor contribution from Sb-$5p_z$ orbitals forming the Γ_8 bands. However, on the contrary, in the high-pressure phase, the VBM and CBM are formed by the Sb-$5p$ and Sb-$5s$ orbitals, respectively, which suggests that at the Γ point the bands get inverted compared to the parent phase. Therefore, from our calculations, it confirms that the relative weights of the Sb-$5s$ and Sb-$5p$ are inverted between the parent ambient phase and high-pressure structure phase, leading to a topological phase transition between the parent ambient topologically nontrivial phase (where $E_{\Gamma_6} - E_{\Gamma_8} < 0$) to the high-pressure topologically trivial phase (where $E_{\Gamma_6} - E_{\Gamma_8} > 0$), which is exactly similar to that of the HgTe/CdTe quantum well [19,24,26]. These preliminary evidences of tuning of the topological features under the application of the uniform

TABLE I. Optimized lattice parameters for the tetragonal unit cell and the corresponding pressure used in the calculations.

a (Å)	c (Å)	Pressure (GPa)
6.20	12.33	0
6.14	12.21	1.4623
6.08	12.08	3.1789
6.01	11.96	4.9569
5.95	11.84	7.2276
5.89	11.71	9.9730
5.83	11.59	12.9749
5.77	11.47	16.0528

hydrostatic pressure further motivates us to analyze the topological signatures, in detail.

V. TOPOLOGICAL INDEXES: THE Z_2 NUMBERS

To ensure the topological character and phase transition, we calculated Z_2 invariant quantities for both parent ambient phase and the high-pressure phases. The corresponding energy difference between Γ_6 and Γ_8 bands ($E_{\Gamma_6} - E_{\Gamma_8}$) as a function of external pressure has been plotted as shown in Fig. 2(c). The light-hole and heavy-hole subbands of Γ_8 symmetry is separated by a small local energy gap at Γ point. Therefore, Z_2 topological invariance can still be defined for the valence bands as they are separated from the conduction bands by local energy gap in the BZ zone around Γ point. We found that the $E_{\Gamma_6} - E_{\Gamma_8}$ is <0 [top inset Fig. 2(c)] and Z_2 invariant quantities (γ; $\gamma_1\gamma_2\gamma_3$) are (1;000) up to the pressure $\approx$6–7 GPa, which indicates its strong topological nature (γ is the strong topological index and γ_i are the three weak topological indices). However, as the pressure increases, the major s-like Γ_6 symmetry bands rise above the Γ_8 bands leading to the $E_{\Gamma_6} - E_{\Gamma_8} > 0$ [see bottom inset Fig. 2(c)]. The Z_2 invariant quantities merged with the topologically trivial value of (0;000), indicating that ZnGeSb$_2$ became a topologically trivial semiconductor by applying moderate hydrostatic pressure. However, increasing pressure further above $\approx$10 GPa, the linear trends of $E_{\Gamma_6} - E_{\Gamma_8}$ follow a downturn. This is associated with the crossing of the top of the valence band (Γ_8) above the Fermi level [see the bottom inset of Fig. 2(c)]. The optimized lattice parameters and corresponding pressures are listed in Table I in Appendix E.

An interesting point to be noted is that this topological phase transition in ZnGeSb$_2$ from topological nontrivial to trivial phases is not due to the breaking of time-reversal symmetry; rather it is protected by time-reversal symmetry. The first hypothetical band structure [Fig. 1(c)] mimics the two times supercell of an ideal cubic HgTe system. By reducing the symmetry of these hypothetical structures further, by setting $\eta \neq 2$ and $x \neq 0.25$, we eventually have the actual ambient structure of ZnGeSb$_2$ [Fig. 1(d)], which has substantial tetragonal distortions as defined in terms of δu's.

Point to be noted is that the calculated Z_2 invariant quantities (1;000) (γ; $\gamma_1\gamma_2\gamma_3$) for both hypothetical band structures and the original band structure of ZnGeSb$_2$ are topologically nontrivial and the reduction of symmetry does not mess up the topological Z_2 invariant characters. For clear visualization we

have shown the evolution of the Wannier charge center (WCC) which is nothing but the Wilson loop shown in Fig. 8. The continuous evolution of WCC governed by time-reversal (TR) symmetry represents a nonzero topological index, opposite to it, which can be considered a normal insulator. In the parent state of ZnGeSb$_2$, the $K_x = 0.5$, $K_y = 0.5$, and $K_z = 0.5$ planes have zero Z_2 invariant, while $K_z = 0$ plane is nontrivial as shown in Fig. 8. For $K_z = 0$ plane, the WCC crosses the reference line for an odd number of times, which results in $Z_2 = 1$. So the topological indices for ZnGeSb$_2$ are (1;000).

Here $\nu_0 = Z_2(K_z = 0.0) = 1$, $\nu_1 = Z_2(K_x = 0.5) = 0$, $\nu_2 = Z_2(K_y = 0.5) = 0$, and $\nu_3 = Z_2(K_z = 0.5) = 0$, as shown in Fig. 8. Under hydrostatic pressure, all $K_z = 0$, $K_x = 0.5$, $K_y = 0.5$, and $K_z = 0.5$ planes have zero Z_2 invariant. So the topological indices for ZnGeSb$_2$ under pressure are (0;000), as shown in Fig. 8.

VI. SPECTRAL FUNCTION AND DIRAC CROSSING

To elucidate our results, we also calculated the spectral distribution at the surface of the semi-infinite slab of ZnGeSb$_2$. Dirac type gapless crossing in the spectral function is a vital hallmark for identifying the topological state and can check the firmness with our previous out-turn of bulk bands. We used Greens function techniques as implemented within the WannierTool [66] for extracting the tight-binding model using maximally projected Wannier functions (WFs). The surface states (SS) emerging from the conduction band (CB) and valence band (VB) exhibit a Dirac-like crossing at the $\bar{\Gamma}$ point in the BZ, as shown in Fig. 3(a), which further ensures the strong topological character in ZnGeSb$_2$. We also calculated spectral distribution at high pressure (7.22 GPa), as shown in Fig. 3(b), where there are clear gaps between valence and conduction bands near the Fermi energy and the absence of any gapless surface states, which further ensure a topologically trivial band insulating phase, at high pressure. This establishes the topological and trivial character in the parent and high-pressure phase in ZnGeSb$_2$. To verify the surface Dirac cone, we also calculated the spectral distribution at the surface time-reversal invariant momenta (TRIM) points scanning the whole BZ in ZnGeSb$_2$ via Greens function techniques as implemented within the PYFPLO module [67,68]. This establishes the strong topological character as surface states have an odd number of Dirac crossings in the parent phase, which goes away at high pressure (see Fig. 9). This ensures the topological phase transition at high pressure in ZnGeSb$_2$.

VII. SPIN-MOMENTUM LOCKING AND BERRY PHASE

The topological nontriviality can be described in the language of spin-momentum locking and the adiabatic quantum phase factor, i.e., the well-known Berry phase, which is picked up during the cyclic adiabatic change of the Hamiltonian [73,74]. Not only that, the spin-momentum locking influences a new type of novel transport phenomenon, robust against impurity scattering and shows weak antilocalization [75]. We also found the signature of the existence of the spin-momentum locking [inset of Fig. 3(c)] in the spin texture at the parent ambient phase and the absence of it in the
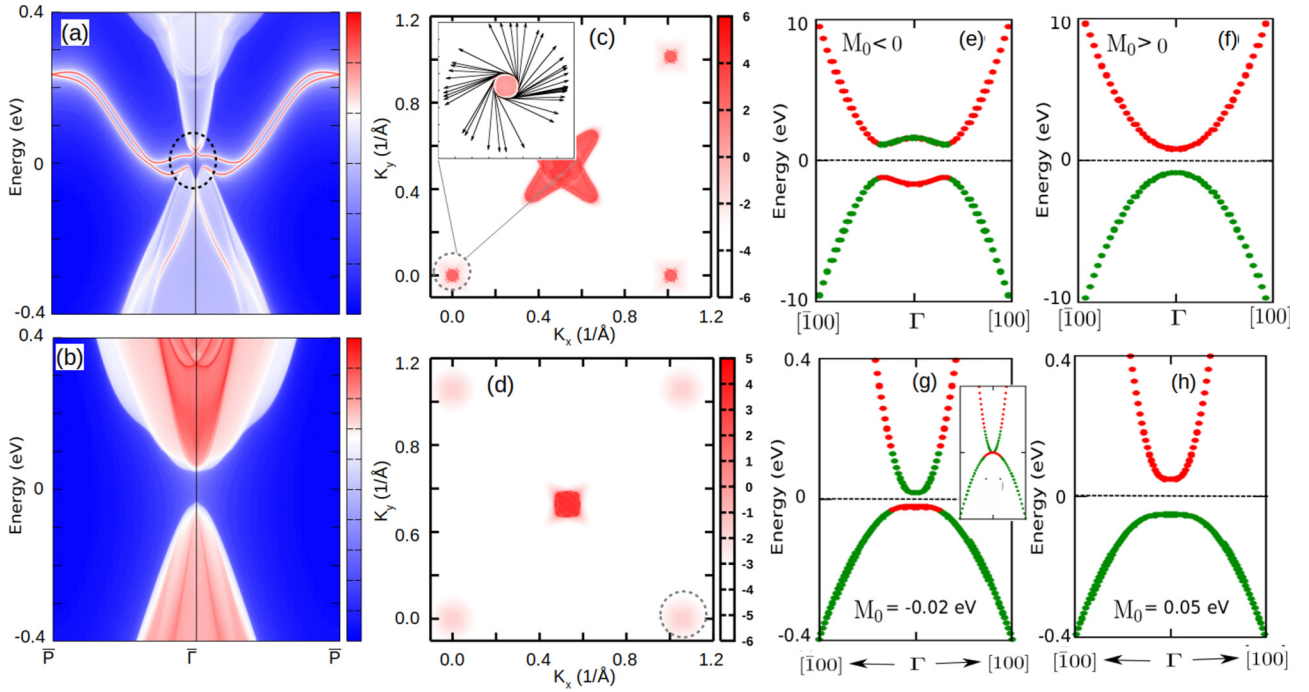
FIG. 3. The surface spectral distribution along the surface BZ for topological (a) nontrivial (ambient pressure) and (b) trivial phases (high pressure). Zero in the energy scale is set at the Fermi energy. (c) and (d) The calculated Berry curvatures and the spin textures for topological nontrivial (parent phase) and trivial phases (high pressure), respectively. Band dispersion obtained from $H(\mathbf{k})$ for (e) $M_0 < 0$ which is in topological phase and (f) $M_0 > 0$ which is in nontopological phase. ZnGeSb$_2$ (g) $M_0 = -0.02$ eV and (h) $M_0 = 0.05$ eV. The inset of figure (g) corresponds to $M_0 = 0$.

high-pressure phase. In the ambient phase of ZnGeSb$_2$, the spin-momentum locking ensures two pairs, $\sigma, \mathbf{k}$ and $-\sigma, -\mathbf{k}$, where $\mathbf{k}$ is the momentum and σ is the spin vector protected by time-reversal symmetry. In other words, we can say that two opposite pairs at the conical dispersion of Dirac cones protected by TR symmetry reflect via spin-momentum locking. Hence, the surface state also agrees well with this result. Therefore, it can be said conclusively that the ambient structure is a strong topological insulator and high-pressure structure is a trivial state of insulator.

We have calculated the Berry phase integrating over Berry curvature in our case. The calculated Berry phase for the parent phase of ZnGeSb$_2$ is very close to 2π (1.995π), which drops down close to zero (0.010π) at about 7 GPa, which suggests that there is a topological phase transition from the topological nontrivial phase at parent phase to the topological trivial band insulating phase at high pressure. To characterize the topological phase in more detail, we have also calculated the Berry curvature and spin texture for the parent and high-pressure phases as shown in Figs. 3(c) and 3(d), respectively. The figures clearly show the changes in Berry curvature by applying the pressure.

VIII. LOW-ENERGY EFFECTIVE MODEL

The topological nature and its effect under hydrostatic pressure in ZnGeSb$_2$ is determined by the physics near the Γ point. Therefore, we have constructed a low-energy effective $\mathbf{k} \cdot \mathbf{p}$ model Hamiltonian considering time-reversal (τ) and spatial [$C_2(x)$, $C_2(y)$, $C_2(z)$, and M_{xy}] symmetries [76] in

ZnGeSb2. The 4×4 Hamiltonian is constructed on the basis of $|\Gamma_6, \Gamma_8; \pm 1/2\rangle = |s, \uparrow\downarrow\rangle$ and $|\Gamma_8; \pm 3/2\rangle = |(p_x \pm ip_y, \uparrow\downarrow\rangle$ of Sb atom. In such a basis set, the Hamiltonian can be written as

$$H(\mathbf{k}) = \begin{pmatrix} \mathcal{M}(\mathbf{k}) & \mathcal{A}(\mathbf{k}) & 0 & -\mathcal{B}^*(\mathbf{k}) \\ \mathcal{A}(\mathbf{k}) & -\mathcal{M}(\mathbf{k}) & \mathcal{B}^*(\mathbf{k}) & 0 \\ 0 & \mathcal{B}(\mathbf{k}) & \mathcal{M}(\mathbf{k}) & \mathcal{A}(\mathbf{k}) \\ -\mathcal{B}(\mathbf{k}) & 0 & \mathcal{A}(\mathbf{k}) & -\mathcal{M}(\mathbf{k}) \end{pmatrix}, \quad (1)$$

with $\mathcal{M}(\mathbf{k}) = M_0 - M_1 k_z^2 - M_2 k_\perp^2$, $\mathcal{A}(\mathbf{k}) = A(k_z^2 - k_+ k_-)$, $\mathcal{B}(\mathbf{k}) = \beta k_+ k_z$, $k_\pm = k_x \pm ik_y$. So the parameters of the low energy effective model are M_{012}, A, and β in which M_0 determines the topology of band structure. This is equivalent to Dirac mass parameter [26,77] and corresponds to the energy difference between basis orbitals. Other parameters are kept fixed in our calculation to reproduce the topological transitions ($M_1 = 1.0$ eV Å^2, $M_2 = -1.0$ eV Å^2, $A = 1.0$ eV Å^2, and $\beta = 1.0$ eV Å^2). The system is in a topological insulating phase when $M_0 M_1 < 0$ and in normal insulating phase when $M_0 M_1 > 0$ as shown in Figs. 3(e) and 3(f). The condition of $M_0 M_1 = 0$ is equivalent to the massless Dirac semimetals description, though the bands have a different physical interpretation.

These situations are similar to the topological phase transition under hydrostatic pressure presented above in Figs. 3(e)–3(h). Such a transition is driven by the sign change of the mass term (M_0) in the three-dimensional Dirac equation, which is the theory of the topological phase transition between the topological nontrivial and trivial insulators. The topological phase in ZnGeSb$_2$ occurs in the inverted regime

where $E_{\Gamma_6} - E_{\Gamma_8} < 0$ and $Z_2 = (1;000)$, then $M_0 < 0$. The topological band ordering can be continuously tuned via moderate hydrostatic pressure until $E_{\Gamma_6} - E_{\Gamma_8} > 0$ and $Z_2 = (0;000)$. Then the mass term M_0 is getting flipped from a negative to a positive value, i.e., $M_0 > 0$ [see Figs. 3(g) and 3(h)]. This corresponds to a phase transition from topological metallic state to a normal insulating phase in ZnGeSb$_2$.

IX. DISCUSSION AND CONCLUSION

The application of the hydrostatic pressure leads to the topological phase transition, which can be understood from the evolution of the tetragonal distortion. Under the application of the hydrostatic pressure, the structural tetragonal distortion decreases, which is quantified by δu terms. The bond lengths and corresponding δu's are shown in Figs. 2(a) and 2(b). The δu decreases, i.e., the strength of tetragonal distortion decreases if we increase pressure. The distortions δu_1 show monotonic fall and δu_2 and δu_3 show monotonic rise with pressure, respectively, however, the δu's have a discontinuous jump at the same pressure range where the band ordering of Γ_8-Γ_6 switches, i.e., at the topological phase transition point. We also found that the increase and jump of the distortions nicely corresponds to the deviation of the Sb atom positions from the ideal value of $x = 0.25$ in the ZnGeSb$_2$ in the body-centered $I\bar{4}2d$ structure, as clearly shown in the inset of Fig. 2(b).

Apparently our findings contradict the results shown in the previous report [42]. Points to be noted here are that, for the chalcopyrite class of materials, both a and c lattice parameters are crucial along with the anion displacement parameter, i.e., the Wyckoff coordinate (x) of the Sb atom in determining the physical properties. We found that the previous [42] studies do not incorporate the effect of the lattice parameter c and the anion displacement factors during the structural evaluation and in the electronic structure. The obtained lattice parameter a in Ref. [42] is in quite good agreement with the value obtained by our calculations; however, we also mentioned the lattice parameter c and free Wyckoff coordinate (x) of the Sb atom obtained through our structural optimization and the energy minimization as shown in Fig. 4 (Appendix A). The calculations also show that by keeping the lattice parameter a fixed, if one changes the lattice parameter c by around 10%, then the electronic structure of the ZnGeSb$_2$ becomes topologically trivial, as shown in Fig. 7, which confirms the importance of the determination of lattice parameter c in determining the topological properties.

In conclusion, ZnGeSb$_2$ is a strained HgTe whose topological band ordering can be tuned by the applications of a moderate perturbation. The parent phase of ZnGeSb$_2$ is a strong topological nontrivial state [$Z_2 = (1;000)$] with an odd number of surface states crossing in the surface BZ. By application of moderate uniform hydrostatic pressure (≈ 7 GPa), ZnGeSb$_2$ undergoes a topological phase transition to the topologically trivial band insulating phase followed by normal metal. The topological phase transition is also associated with the tetragonal distortions (δu) in ZnGeSb$_2$. With increasing the pressure, the structural distortion parameters (δu) are decreasing and at the critical pressure of the pressure transition, there is a jump in the δu. The topological phase
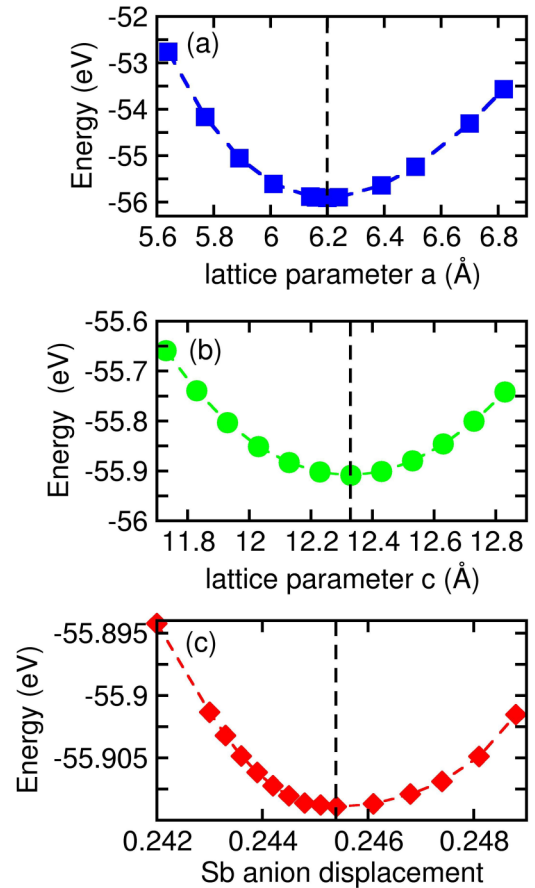

FIG. 4. Total energy calculations as a function of the lattice parameters (a) a and (b) c, respectively. (c) Total energy calculations as a function of the Wyckoff free coordinate x of the Sb atoms. Energetically minimized values are marked by the dotted vertical lines in each plots.

transition is associated with the change in the wave function parity of Γ_6-Γ_8 band and the sign of the mass term at the Γ point in the BZ caused by the structural distortion. The odd number of Dirac crossing in the surface spectral function and the spin-momentum locking makes ZnGeSb$_2$ very useful for studying the interplay effect in future for topological transport [79,80].

Our theoretical results not only predict many existing properties in a material from the chalcopyrite family having low band inversion strength, but also shows how the complex interplay between structural parameters (as anionic Wyckoff position depends on structural parameters for this family) and properties leads to topological phase transition in noncentrosymmetric ZnGeSb$_2$ which can be exploited to overcome the challenges and limitations for its realization of topological signature in experiment using state-of-art equipment taking pressure as a probe [35,81]. Also as ZnGeSb$_2$ breaks inversion symmetry, it is possible to generate the nonlinear Hall effect due to the Berry curvature dipole in its topological phase [82,83]. The nonlinear phenomenon can be thought of as a current-induced anomalous Hall effect and can be utilized as an energy-harvesting mechanism based on the anomalous Nernst and photovoltaic effect [84]. This part

is beyond the scope of our current paper and is a subject of future study. We believe that our detailed and systematic study on a topological quantum material ZnGeSb$_2$ from the chalcopyrite family paves the way for future experimental and theoretical exploration, and will be of interest to a wide range of theorists and experimentalists within the condensed matter community for its potential application in the field of anomalous photovoltaic and thermoelectric response.

APPENDIX A: ENERGY MINIMIZATION CALCULATIONS OF STRUCTURAL PARAMETERS

Energy minimization of structural parameters viz. lattice parameters a, c, and free Wyckoff position of the Sb atoms as described in Sec. II, shown in Fig. 4. The detailed

FIG. 6. (a) and (b) Ambient (topological nontrivial) and (c) and (d) high-pressure (topological trivial) phases of ZnGeSb$_2$, respectively, for the the projected bands of Sb-5p_y and Sb-5p_z, respectively. Γ_8 band characters are marked in the figure and the band inversion in topological phase happens between 5s (Γ_6) and 5p (Γ_8) orbitals at the Γ point in the BZ. Fermi energy set at zero on the energy axis.

first-principles calculations are done with this optimized and energy minimized structural parameters.

APPENDIX B: THERMODYNAMIC AND DYNAMICAL STABILITY

In order to establish the calculated results, the stability of the compound is very important to examine.
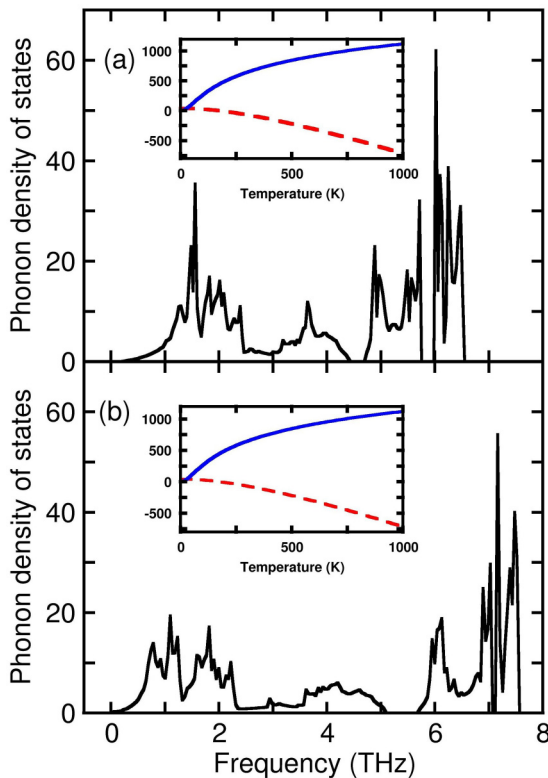

FIG. 5. The calculated phonon density of states for the (a) parent structure and (b) high-pressure structure are shown. The inset of the two panels shows the calculated entropy (solid line) in the unit of J/K mol and the Helmholtz free energy (dotted line) in unit of kJ/mol.
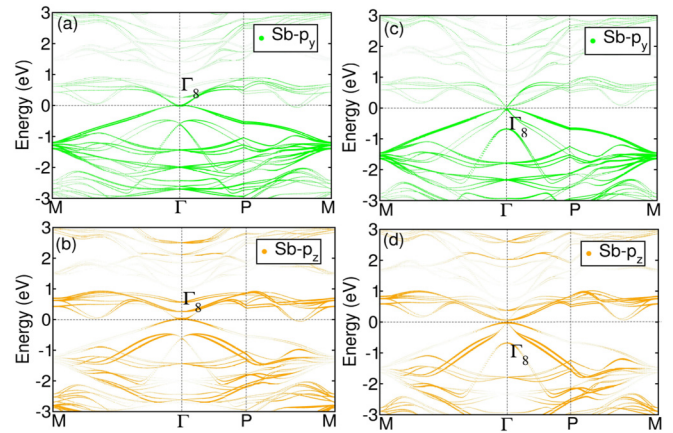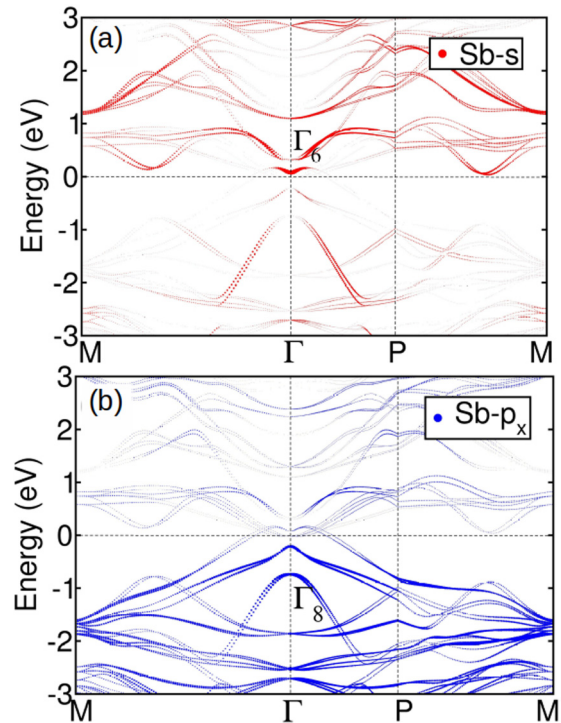
FIG. 7. The orbital projected bands of (a) Sb-s and (b) Sb-p_x, for the ZnGeSb$_2$, with 10% reduced c lattice parameter, keeping a the same as that of the equilibrium value of the lattice parameter. Fermi energy set at zero on the energy axis.
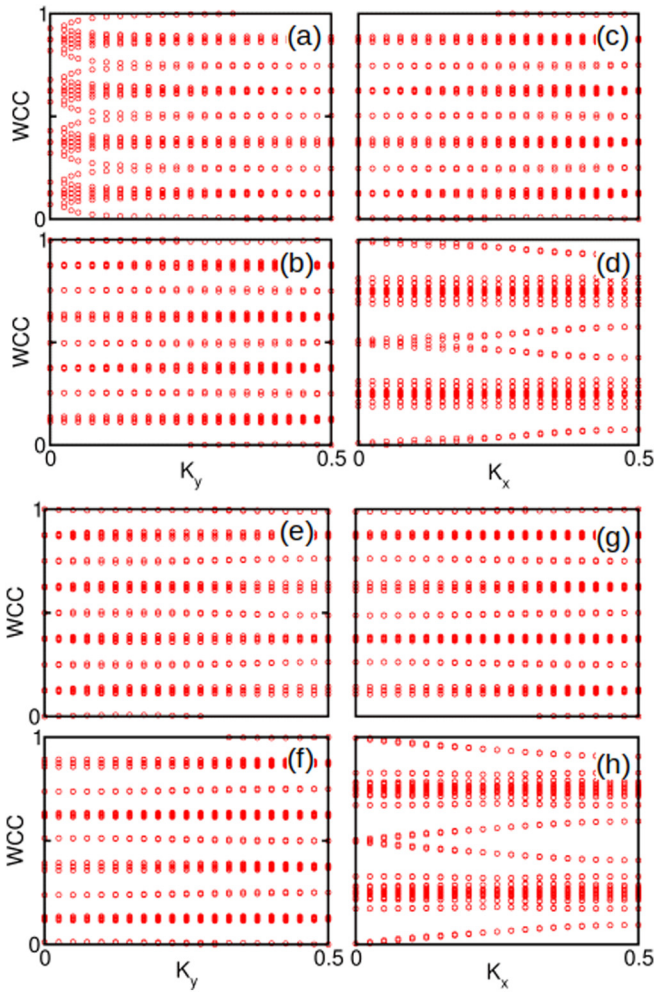
FIG. 8. The flow chart of the average position of Wannier charge centers (WCCs) obtained by the Wilson-loop method for the highest occupied valence band for parent state (top panel, (a)–(d)) and high-pressure phase (bottom panel, (e)–(h)) of ZnGeSb$_2$. (a) (d) and (e)–(h) are the calculated WCC for ambient and high pressure phases respectively for the four time-reversal invariant planes $K_x = 0.0$, $K_x = 0.5$, $K_y = 0.5$, $and K_z = 0.5$, respectively.
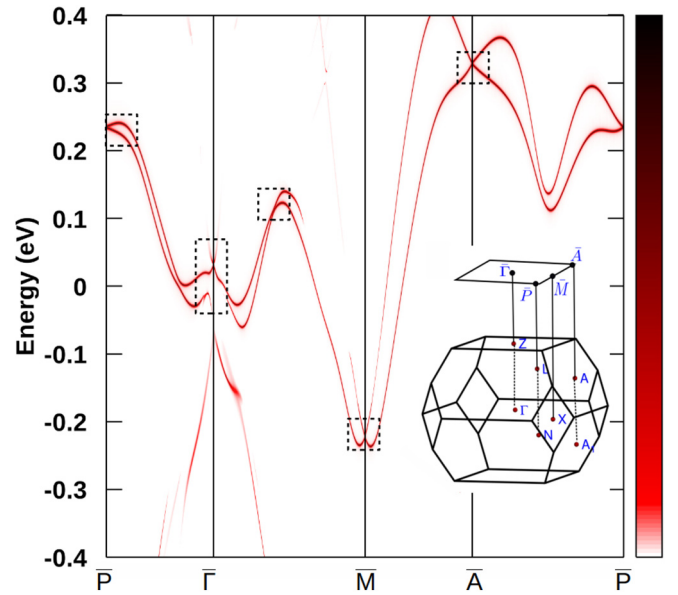

FIG. 9. Spectral distribution along the surface Time-reversal invariant points (TRIM) points for topological nontrivial (ambient pressure). Inset shows TRIM in the BZ in ZnGeSb$_2$ and its surface projection. The dotted boxes are shown at the places of the Dirac crossing in the spectral function.

ing thermodynamic stability for both parent ambient phase as well as the high-pressure phase.

APPENDIX C: PROJECTED BAND STRUCTURES FOR AMBIENT AND HIGH-PRESSURE PHASE

This Appendix shows the projected bands of Sb-5p_y and Sb-5p_z in ZnGeSb$_2$ at both topological and trivial phases, as shown in Fig. 6. Figure 7 ensures that the lattice parameter c along the easy axis is an important structural parameter in determining the ground state whether it is in topological or trivial phase. 10% reduction of lattice parameter c, keeping the other structural parameters the same as that of the equilibrium value, ZnGeSb$_2$ switches to trivial phase from its topological ground state.

APPENDIX D: WANNIER CHARGE CENTER CALCULATIONS AND SURFACE STATES

Here we calculate the topological Z_2 invariant for noncentrosymmetric crystal ZnGeSb$_2$ using the Wannier charge center (WCC) algorithm as shown in Fig. 8. The tight-binding model has been extracted using maximally projected Wannier functions (WFs) for the Zn-3d, Ge-3d, Ge-4s, Ge-4p, and Sb-5p orbitals. The topology comes at Γ point where band inversion happens from this band for which we are interested to calculate Z_2 in ZnGeSb$_2$. The WCC are calculated in momentum space by considering four time-reversal invariant planes $K_x = 0.5$, $K_y = 0.5$, $K_z = 0.5$, and $K_z = 0.0$ in the three-dimensional BZ. For example, the $K_z = 0.0$ plane goes through the origin and spanned by reciprocal lattice vector $\mathbf{G_1}$-$\mathbf{G_2}$, whereas $K_z = 0.5$ plane goes through the $\mathbf{G_3}$ and spanned by reciprocal lattice vector $\mathbf{G_1}$-$\mathbf{G_2}$.

It becomes very necessary when the material is not yet synthesized experimentally. Therefore, we examine the dynamical stability through the calculated phonon density of states, whereas the thermodynamic stability via calculating the Helmholtz free energy and the entropy as shown in Fig. 5. We have calculated the phonon frequencies via finite displacement method using the first-principles derived Hessian matrix. The thermodynamic quantities can be obtained through the phonon energy by integrating the phonon frequencies over the entire Brillouin zone under harmonic approximation [78].

The calculations show that the absence of any imaginary frequency mode in the phonon density of states confirms the dynamical stability of the both parent and high-pressure phase of ZnGeSb$_2$. Moreover, the calculated Helmholtz free energy remains negative in the entire temperature range, whereas the entropy of the system increases with the temperature, suggest-

The calculated spectral distribution at the surface time-reversal invariant momenta (TRIM) points in ZnGeSb$_2$. The surface states (SS) emerging from the conduction band (CB) and valence band (VB) at Γ point in the BZ cross an odd number of times (5 times of Dirac crossing) shown in Fig. 9 which ensures the strong topological character. Point to be noted that the crossing do not always appear at the TRIM points due to the breaking of inversion symmetry in ZnGeSb$_2$ structure.

APPENDIX E: DETAILS OF THE OPTIMIZED LATTICE PARAMETERS

We have shown the optimized lattice parameters and the corresponding pressures in Table I.

[1] J. Hu, S.-Y. Xu, N. Ni, and Z. Mao, Annu. Rev. Mater. Res. **49**, 207 (2019).

[2] M. He, H. Sun, and Q. L. He, Front. Phys. **14**, 43401 (2019).

[3] M. Kim, Z. Jacob, and J. Rho, Light Sci. Appl. **9**, 130 (2020).

[4] B. J. Wieder, B. Bradlyn, J. Cano, Z. Wang, M. G. Vergniory, L. Elcoro, A. A. Soluyanov, C. Felser, T. Neupert, N. Regnault, and B. A. Bernevig, Nat. Rev. Mater. **7**, 196 (2022).

[5] N. Kumar, S. N. Guin, K. Manna, C. Shekhar, and C. Felser, Chem. Rev. **121**, 2780 (2021).

[6] B. Yan and C. Felser, Annu. Rev. Condens. Matter Phys. **8**, 337 (2017).

[7] B. A. Bernevig, C. Felser, and H. Beidenkopf, Nature (London) **603**, 41 (2022).

[8] D.-W. Zhang, Y.-Q. Zhuc, Y. X. Zhaoc, H. Yana, and S.-L. Zhua, Adv. Phys. **67**, 253 (2019).

[9] Y. Liu, X. Chen, and Y. Xu, Adv. Funct. Mater. **30**, 1904784 (2020).

[10] P. Liu, J. R. Williams, and J. J. Cha, Nat. Rev. Mater. **4**, 479 (2019).

[11] Y. Tokura, K. Yasuda, and A. Tsukazaki, Nat. Rev. Phys. **1**, 126 (2019).

[12] S.-Y. Yang, H. Yang, E. Derunova, S. S. P. Parkin, B. Yan, and M. N. Ali, Adv. Phys.: X **3**, 1414631 (2018).

[13] H. Gao, J. W. F. Venderbos, Y. Kim, and A. M. Rappe, Annu. Rev. Mater. Res. **49**, 153 (2019).

[14] J. Liu, Comput. Mater. Sci. **195**, 110467 (2021).

[15] J. Xiao and B. Yan, Nat. Rev. Phys. **3**, 283 (2021).

[16] J. Maciejko, T. L. Hughes, and S.-C. Zhang, Ann. Rev. Cond. Mat. Phys. **2**, 31 (2011).

[17] D. Abergel, Nat. Phys. **14**, 108 (2018)

[18] M. Z. Hasan and J. E. Moore, Annu. Rev. Condens. Matter Phys. **2**, 55 (2011).

[19] A. Bernevig, T. Hughes, and S. C. Zhang, Science **314**, 1757 (2006).

[20] Q. Xiao-Liang and S.-C. Zhang, Phys. Today **63**(1), 33 (2010).

[21] M. Z. Hasan and C. L. Kane, Rev. Mod. Phys. **82**, 3045 (2010).

[22] J. E. Moore, Nature (London) **464**, 194 (2010).

[23] J. E. Moore and L. Balents, Phys. Rev. B **75**, 121306(R) (2007).

[24] L. Fu, C. L. Kane, and E. J. Mele, Phys. Rev. Lett. **98**, 106803 (2007).

[25] R. Roy, Phys. Rev. B **79**, 195322 (2009).

[26] M. König, S. Wiedmann, C. Brüne, A. Roth, H. Buhmann, L. Molenkamp, X.-L. Qi, and S.-C. Zhang, Science **318**, 766 (2007).

[27] M. Novak, S. Sasaki, K. Segawa, and Y. Ando, Phys. Rev. B **91**, 041203(R) (2015).

[28] B. Singh, A. Sharma, H. Lin, M. Z. Hasan, R. Prasad, and A. Bansil, Phys. Rev. B **86**, 115208 (2012).

[29] M. Orlita, D. M. Basko, M. S. Zholudev, F. Teppe, W. Knap, V. I. Gavrilenko, N. N. Mikhailov, S. A. Dvoretskii, P. Neugebauer, C. Faugeras *et al.*, Nat. Phys. **10**, 233 (2014).

[30] M. Yang, Y. Z. Luo, M. G. Zeng, L. Shen, Y. H. Lu, J. Zhou, S. J. Wang, I. K. Souf, and Y. P. Feng, Phys. Chem. Chem. Phys. **19**, 29372 (2017).

[31] M. Zhang, X. Wang, A. Rahman, Q. Zeng, D. Huang, R. Dai, Z. Wang, and Z. Zhang, Appl. Phys. Lett. **112**, 041907 (2018).

[32] X. Xi, C. Ma, Z. Liu, Z. Chen, W. Ku, H. Berger, C. Martin, D. B. Tanner, and G. L. Carr, Phys. Rev. Lett. **111**, 155701 (2013).

[33] J. I. Facio, D. Efremov, K. Koepernik, J.-S. You, I. Sodemann, and J. van den Brink, Phys. Rev. Lett. **121**, 246403 (2018).

[34] X. Xi, X.-G. He, F. Guan, Z. Liu, R. D. Zhong, J. A. Schneeloch, T. S. Liu, G. D. Gu, X. Du, Z. Chen, X. G. Hong, W. Ku, and G. L. Carr, Phys. Rev. Lett. **113**, 096401 (2014).

[35] A. Ohmura, Y. Higuchi, T. Ochiai, M. Kanou, F. Ishikawa, S. Nakano, A. Nakayama, Y. Yamada, and T. Sasagawa, Phys. Rev. B **95**, 125203 (2017).

[36] L. Zhao, J. Wang, B.-L. Gu, and W. Duan, Phys. Rev. B **91**, 195320 (2015).

[37] Z. Guguchia, A. M. dos Santos, F. O. von Rohr, J. J. Molaison, S. Banerjee, D. Rhodes, J. Yin, R. Khasanov, J. Hone, Y. J. Uemura, M. Z. Hasan, H. Luetkens, E. S. Bozin, and A. Amato, J. Phys. Soc. Jpn. **89**, 094707 (2020).

[38] T. Ideue, M. Hirayama, H. Taiko, T. Takahashi, M. Murase, T. Miyake, S. Murakami, T. Sasagawa, and Y. Iwasa, Proc. Natl. Acad. Sci. USA **116**, 25530 (2019).

[39] P. Barone, T. Rauch, D. Di Sante, J. Henk, I. Mertig, and S. Picozzi, Phys. Rev. B **88**, 045207 (2013).

[40] R. Juneja, R. Shinde, and A. K. Singh, J. Phys. Chem. Lett. **9**, 2202 (2018).

[41] J. Li, Y. Li, S. Du, Z. Wang, B.-L. Gu, S.-C. Zhang, K. He, W. Duan, and Y. Xu, Sci. Adv. **5**, eaaw5685 (2019).

[42] W. Feng, D. Xiao, J. Ding, and Y. Yao, Phys. Rev. Lett. **106**, 016402 (2011).

[43] P. C. Sreeparvathy, V. Kanchana, G. Vaitheeswaran, and N. E. Christensen, Phys. Chem. Chem. Phys. **18**, 26275 (2016).

[44] I. V. Korobeinikov, N. V. Morozova, L. N. Lukyanova, O. A. Usov, V. A. Kulbachinskii, V. V. Shchennikov, and S. V. Ovsyannikov, J. Phys. D: Appl. Phys. **51**, 025501 (2018).

[45] Y. Yuan, X. Zhu, Y. Zhou, X. Chen, C. An, Y. Zhou, R. Zhang, C. Gu, L. Zhang, X. Li, and Z. Yang, NPG Asia Mater. **13**, 15 (2021).

[46] T. Wen, Y. Wang, N. Li, Q. Zhang, Y. Zhao, W. Yang, Y. Zhao, and Ho-k. Mao, J. Am. Chem. Soc. **141**, 505 (2019).

[47] J. Ruan, S.-K. Jian, D. Zhang, H. Yao, H. Zhang, S. C. Zhang, and D. Xing, Phys. Rev. Lett. **116**, 226801 (2016).

[48] G. A. Medvedkin, T. Ishibashi, T. Nishi, K. Hayata, Y. Hasegawa, and K. Sato, Jpn. J. Appl. Phys. **39**, L949 (2000).

[49] S. Cho, S. Choi, G.-B. Cha, S. C. Hong, Y. Kim, Y.-J. Zhao, A. J. Freeman, J. B. Ketterson, B. J. Kim, Y. C. Kim, and B.-C. Choi, Phys. Rev. Lett. **88**, 257203 (2002)

[50] S. C. Erwin, and Ž. Igor, Nat. Mater. **3**, 410 (2004).

[51] B. Sadhukhan, Y. Zhang, R. Ray, and J. van den Brink, Phys. Rev. Materials **4**, 064602 (2020).

[52] K. Inzani, A. Faghaninia, and S. M. Griffin, Phys. Rev. Research **3**, 013069 (2021).

[53] R. Cao, H.-X. Deng, J.-W. Luo, and S.-H. Wei, J. Semicond. **40**, 042102 (2019).

[54] J. Gooth, G. Schierning, C. Felser, and K. Nielsch, MRS Bull. **43**, 187 (2018).

[55] N. Xu, Y. Xu, and J. Zhu, npj Quantum Mater. **2**, 51 (2017).

[56] Z.-Y. Fang, D. Ye, Y.-Y. Zhang, and Z.-X. Hu, Phys. Rev. B **103**, 235161 (2021).

[57] D. Baldomir and D. Faílde, Sci. Rep. **9**, 6324 (2019).

[58] C. Fua, Y. Sun, and C. Felser, APL Mater. **8**, 040913 (2020).

[59] Te-H. Liu, J. Zhou, and M. Li, Proc. Natl. Acad. Sci. USA **115**, 879 (2018).

[60] J. P. Perdew, K. Burke, and M. Ernzerhof, Phys. Rev. Lett. **77**, 3865 (1996).

[61] G. Kresse and J. Hafner, Phys. Rev. B **47**, 558(R) (1993).

[62] G. Kresse and J. Furthmuller, Phys. Rev. B **54**, 11169 (1996).

[63] N. Marzari and D. Vanderbilt, Phys. Rev. B **56**, 12847 (1997).

[64] I. Souza, N. Marzari, and D. Vanderbilt, Phys. Rev. B **65**, 035109 (2001).

[65] G. Pizzi, V. Vitale, R. Arita, S. Blügel, F. Freimuth, G. Géranton, M. Gibertini, D. Gresch, C. Johnson, T. Koretsune *et al.*, J. Phys.: Condens. Matter **32**, 165902 (2020).

[66] Q. Wu, S. Zhang, H.-F. Song, M. Troyer, and A. A. Soluyanov, Comput. Phys. Commun. **224**, 405 (2018).

[67] K. Koepernik and H. Eschrig, Phys. Rev. B **59**, 1743 (1999).

[68] https://www.fplo.de.

[69] J. M. Luttinger and W. Kohn, Phys. Rev. **97**, 869 (1955).

[70] G. Bir and G. Pikus, *Symmetry and Strain-Induced Effects in Semiconductors* (Wiley, New York, 1974).

[71] M. S. Dresselhaus, G. Dresselhaus, and A. Jorio, *Group Theory (Application to the Physics of Condensed Matter)* (Springer, Berlin, 2008).

[72] L. C. L. Y. Voon, and M. Willatzen, *The k·p Method* (Springer, Berlin, 2009).

[73] M. V. Berry, Proc. R. Soc. London Ser. A **392**, 45 (1984).

[74] D. Xiao, M.-C. Chang, and Q. Niu, Rev. Mod. Phys. **82**, 1959 (2010).

[75] D. Baykusheva, A. Chacón, J. Lu, T. P. Bailey, J. A. Sobota, H. Soifer, P. S. Kirchmann, C. Rotundu, C. Uher, T. F. Heinz, D. A. Reis, and S. Ghimire, Nano Lett. **21**, 8970 (2021).

[76] D. Varjas, T. Rosdahl, A. R Akhmerov, New J. Phys. **20**, 093026 (2018).

[77] I. Yu. Sklyadneva, P. Rusinov, R. Heid, K.-P. Bohnen, P. M. Echenique, and E. V. Chulkov, Sci. Rep. **6**, 24137 (2016).

[78] A. Togo, and I. Tanaka, Scr. Mater. **108**, 1 (2015).

[79] Y. Araki, Ann. Phys. (Berlin) **532**, 1900287 (2020).

[80] M. Lin, I. Robredo, N. B. M. Schroter, C. Felser, M. G. Vergniory, and B. Bradlyn, arXiv:2204.10113.

[81] Z. Xu, M. Ye, J. Li, W. Duan, and Y. Xu, Phys. Rev. B **105**, 085129 (2022).

[82] I. Sodemann and L. Fu, Phys. Rev. Lett. **115**, 216806 (2015).

[83] Y. Zhang and L. Fu, Proc. Natl. Acad. Sci. **118**, e2100736118 (2021).

[84] M. Mizuguchi and S. Nakatsuji, Sci. Tech. Adv. Mater. **20**, 262 (2019).